ORIGINAL PAPER

Formation of free-surface vortex and vortex suppression by rotating stopper-rod at end of tundish casting

Qing Fang[1,2] · Peng Zhao[1,3] · Hua Zhang[1,3] (ID) · Wen-hao Zhou[2] · Gang Yu[2] · Jia-hui Wang[1,3] · Hong-wei Ni[1,3]

Abstract

A rotating stopper-rod technique was proposed to suppress the formation of free-surface vortex in the tundish. The large eddy simulation model coupled with volume of fluid model was developed to study the steel–slag–gas three-phase flow behavior. The critical slag entrapment height of the free-surface vortex and mass of residual steel were predicted at different rotating speeds (30, 60, 90 and 120 r/min) of the rotating stopper-rod. The numerical model was verified by water model experiment. The results showed that by rotating the stopper-rod in the opposite direction of the vortex above the submerged entry nozzle, the formation of vortex can be effectively disturbed and the critical height of the free-surface vortex can be reduced. Particularly for the 2nd strand, when the rotating speeds are 30, 60, 90 and 120 r/min, the critical height of the free-surface vortex above the 2nd strand is 7.3, 4.7, 6.3 and 7.4 cm, respectively. A reasonable rotating speed should be 60 r/min, which can reduce about 2 tons of residual steel. Other rotating speeds just can reduce about 1.6 tons of residual steel.

Keywords Tundish · Free-surface vortex · Stopper-rod · Numerical simulation · Multiphase flow

1 Introduction

The slag entrapment by free-surface vortex is one of the main sources of inclusions during the casting process, which will cause product quality defects in steel products [1–3]. At the end of the pouring period, the molten steel level keeps decreasing and free-surface vortex is formed above the submerged entry nozzle (SEN). Meanwhile, the covering slag, air and agglomerated inclusions enter into the SEN with the vortex, which will reduce the cleanliness of the steel, block the SEN and deteriorate the quality of

the cast billet. The formation of free-surface vortex in tundish is related to the conservation of angular momentum [4]. Many scholars pointed out that the formation of the free-surface vortex in the ladle during draining process is related to the initial perturbation [5–7], which provides initial angular momentum to the molten steel. In tundish, it has a certain tangential velocity when the molten steel flows to the SEN due to flow control devices, and finally forms free-surface vortex. With regard to the influence of Coriolis force in the formation of free-surface vortex, the time scale of molten steel flowing in tundish is small. The major factor is the initial tangential velocity.

A precautionary measure is to stop draining before the liquid level reaches the critical height of the formation of free-surface vortex, while it will cause a large mass of residual steel, and the economic benefit is low. Thus, it is essential to develop effective methods to suppress free-surface vortex. However, there are few researches on the suppression of free-surface vortex in tundish. Ruan et al. [8] found that the critical height was effectively reduced by changing the dam orifices directly toward the stopper-rod, but changing the position of dam orifices should be verified

✉ Hua Zhang
huazhang@wust.edu.cn

1　The State Key Laboratory of Refractories and Metallurgy, Wuhan University of Science and Technology, Wuhan 430081, Hubei, China

2　Hunan Valin Xiangtan Iron and Steel Co., Ltd., Xiangtan 411101, Hunan, China

3　Hubei Provincial Key Laboratory for New Processes of Ironmaking and Steelmaking, Wuhan University of Science and Technology, Wuhan 430081, Hubei, China

to ensure that the flow field at steady-state is not negatively affected. Xuan et al. [9] investigated the effect of casting speed and square baffle nozzle on the critical height in a three-strand tundish and found that the asymmetric distribution of the free-surface high-speed region is the source of vortex formation, and the critical height can be reduced by using the square baffle nozzle and low casting speed. Wang et al. [10] found that blowing argon to make molten steel fluctuate in the ladle can interfere with the formation of free-surface vortex. Anti-vortex researches have been carried out by scholars in other fields. Khadem Rabe et al. [11] investigated a funnel device installed above the outlet and found that the funnel could inhibit the accumulation of vortices, which led to a decrease in vortex intensity. Gao et al. [12] studied a vertical pipe inlet/outlet with a horizontal anti-vortex plate and optimized its diversion orifices heights and divergence angles. In this paper, a rotating stopper-rod technique is proposed to disturb the formation of the free-surface vortex. When the molten steel is at a low level, the stopper-rod rotates in the opposite direction to the vortex direction to disturb the formation of free-surface vortex above the SEN. The proposed method can effectively reduce the critical height of the free-surface vortex without affecting the flow field during casting process of tundish.

Previously, the k–ε turbulent model is usually applied to calculate the steady and transient casting process in tundish [13, 14], which assumes that turbulent flow is isotropic and abandons the simulation of unsteady turbulent flow information. Recently, the large eddy simulation (LES) method is more and more frequently applied for calculating the transient turbulent behaviors in casting process with slag entrapment [15–21], which is proved to be more accurate to capture multi-scale vortices [22]. Alkishriwi et al. [23] used the LES model to simulate the tundish flow field and verified it by particle image velocimetry (PIV), proving that the main characteristics of the flow were consistent between the results of LES model and PIV, and the funnel-shaped vortex could be well captured by LES model.

In this paper, the flow field of molten steel in a two-strand slab casting tundish at steady-state casting period was firstly calculated by k–ε turbulent model to obtain the initial flow pattern for the calculation of free-surface vortex. Then, the LES coupled with volume of fluid (VOF) model was developed to investigate the three-phase (steel–slag–air) flow behavior during draining process at the end of casting sequence, and the formation mechanism of free-surface vortex and suppression effect of the proposed rotating stopper-rod with different rotating speeds were analyzed and compared. Besides, the numerical model was

verified by water model experiments with the same operation conditions. The present study can not only offer a deeper understanding of free-surface vortex formation at the end of casting sequence in tundish, but also provide an effective method for suppressing the free-surface in the tundish.

2 Model description

2.1 Basic assumptions

Due to the complexity of the fluid flow in tundish at the end of casting sequence, the following assumptions are considered during the multiphase moldering of free-surface vortex:

(1) The influence of temperature on the fluid flow is ignored;
(2) The fluid flow is viscous and incompressible flow;
(3) The casting speed variations during draining process are ignored, and the velocities at outlets remain constant during the whole steady-state and transient casting process;
(4) The surface tensions between every contact two phases were considered;
(5) Only one-way coupling was considered, that is, ignoring the effect of the fluids on the stopper-rod;
(6) The initial flow conditions for the calculation of multiphase flow at the end of tundish casting sequence are obtained by the calculation of steady-state casting.

2.2 Governing equations

The drop of molten steel level at the end of tundish casting sequence is calculated by a coupled mathematical model, which is on tracking the steel–slag interface to obtain the shape of free-surface vortex. The simulation used LES coupled with VOF model, and the control equations are shown as follows.

2.2.1 Turbulence model

Implicit filtering is performed on the continuity equation and the momentum equation, and the filtered equations are presented as follows [24, 25]:

$$\frac{\partial \overline{u}_i}{\partial x_i} = 0 \tag{1}$$

$$\frac{\partial \overline{u}_i}{\partial t} + \frac{\partial}{\partial x_j}\left(\overline{u}_i \overline{u}_j\right) = -\frac{1}{\rho}\frac{\partial \overline{p}}{\partial x_i} + \mu \frac{\partial}{\partial x_j}\left(\frac{\partial \overline{u}_i}{\partial x_j} + \frac{\partial \overline{u}_j}{\partial x_i}\right) + \frac{\partial \tau_{\text{sgs}}}{\partial x_j} \tag{2}$$

where ρ is the density, kg m^{-3}; t is the time, s; x_i and x_j are the distance of the ith and jth orthogonal direction, respectively, m; μ is the dynamic viscosity, kg/(m s); $\overline{u}_i$ and $\overline{u}_j$ are the velocity component along the ith and jth orthogonal direction, respectively, m s^{-1}; and $\overline{p}$ is the filtered pressure, Pa. In LES model, the small-scale eddies are modeled by using the subgrid-scale (SGS) model. τ_{sgs} is the subgrid-scale stress tensor, which is defined by Eq. (3):

$$\tau_{\text{sgs}} = \overline{u}_i\,\overline{u}_j - \overline{u_i u_j} \tag{3}$$

In this paper, the wall-adapting local eddy-viscosity (WALE) model was used, which is believed to be reasonable and accurate in flows associated with complicate geometries [26]. In WALE model, the turbulent viscosity (v_{sgs}) is modeled by [26, 27]:

$$v_{\text{sgs}} = \rho L_s^2 \frac{\left(S_{ij}^{\text{d}} S_{ij}^{\text{d}}\right)^{3/2}}{\left(\overline{S}_{ij}\overline{S}_{ij}\right)^{5/2} + \left(S_{ij}^{\text{d}} S_{ij}^{\text{d}}\right)^{5/4}} \tag{4}$$

where L_s and S_{ij}^{d} in the WALE model are defined, respectively, as

$$L_s = \min(\kappa d,\ C_w V^{1/3}) \tag{5}$$

$$S_{ij}^{\text{d}} = \frac{1}{2}\overline{g}_{ij}^2 + \overline{g}_{ji}^2 - \frac{1}{3}\delta_{ij}\overline{g}_{kk}^2 \tag{6}$$

$$\overline{g}_{ij} = \frac{\partial \overline{u}_i}{\partial x_j},\ \overline{g}_{ji} = \frac{\partial \overline{u}_j}{\partial x_i} \tag{7}$$

$$\overline{S}_{ij} = \frac{1}{2}\left(\frac{\partial \overline{u}_i}{\partial x_j} + \frac{\partial \overline{u}_j}{\partial x_i}\right) \tag{8}$$

where d is the distance from the cell center to the closest wall, m; V is the cell volume; δ_{ij} is the Kronecker delta function; $\overline{g}_{ij}$ and $\overline{g}_{ji}$ represent the characteristic strain rate tensor associated with the wall-adjacent region; $\overline{g}_{kk}$ is the trace of the filtered rate-of-strain tensor; κ is the von Kármán constant, and the chosen value is 0.41; and C_w is chosen as 0.325, which has shown consistently superior results in ANSYS Fluent.

2.2.2 VOF model

Since the air, slag and molten steel are not miscible with each other, the VOF model is chosen for the multiphase flow model to solve the distribution of each phase. The VOF model can trace the phase interfaces to obtain a clear vortex shape. The interface between phases is accomplished by solving the continuity equation for the volume fraction of multiple phases.

For the qth phase, the continuity equation is given in Eq. (9) [28]:

$$\frac{1}{\rho_q}\left[\frac{\partial}{\partial t}\left(\alpha_q \rho_q\right) + \nabla\left(\alpha_q \rho_q \vec{u}_q\right) = S_{\alpha_q} + \sum_{p=1}^{n}\left(m_{\overrightarrow{pq}} - m_{\overrightarrow{qp}}\right)\right] \tag{9}$$

where ρ_q is the density of phase q, kg m^{-3}; α_q is the volume fraction of phase q in the control cell; $\vec{u}_q$ is the velocity of phase q, m s^{-1}; $m_{\overrightarrow{pq}}$ is the mass transfer from phase q to phase p; $m_{\overrightarrow{qp}}$ is the mass transfer from phase p to phase q, kg; S_{α_q} is the source term, of which the value is 0 by default; and n is the number of the phases.

The volume fraction equation will not be solved for primary phase and it is computed based on the following constraint. The relationship among air, slag and molten steel is shown in Eq. (10):

$$\alpha_{\text{air}} + \alpha_{\text{slag}} + \alpha_{\text{steel}} = 1 \tag{10}$$

2.3 Initial and boundary conditions

In this research, a two-strand slab casting tundish is chosen as the research subject and the three-dimensional structure of the tundish is shown in Fig. 1. The left and right parts of tundish are symmetrical. Table 1 lists the main industrial conditions and physical parameters of the tundish applied in the calculations.

In recent years, when scholars study the mold, they found that the mold with symmetrical structure will have asymmetric flow field after using LES [21]. Therefore, the full-scale model of the tundish is applied for the numerical simulation in this paper. The computational domain is divided into upper and lower parts, the upper part represents area of slag phase, and the rest is the molten steel phase. The LES model has requirements for the boundary layer grid and usually controls the y^+ value at 1. However, considering the computational efficiency, the Werner-Wengle wall function is used to control the y^+ value to be around 30. When simulating the rotation of the stopper-rod at the end of the tundish casting sequence, the sliding mesh technique is used to realize the stopper-rod rotation. Therefore, the entire computational domain is divided into two domains containing both stationary and rotating regions, with a total of about 3,660,000 hexahedral structure meshes, as shown in Fig. 2, in which the local refinement technique is used to more accurately calculate the multiphase flow behaviors in the tundish during the draining process, especially when the stopper-rod is rotated.

The initial conditions of turbulence and multiphase flow for calculating the multiphase flow behaviors in the tundish
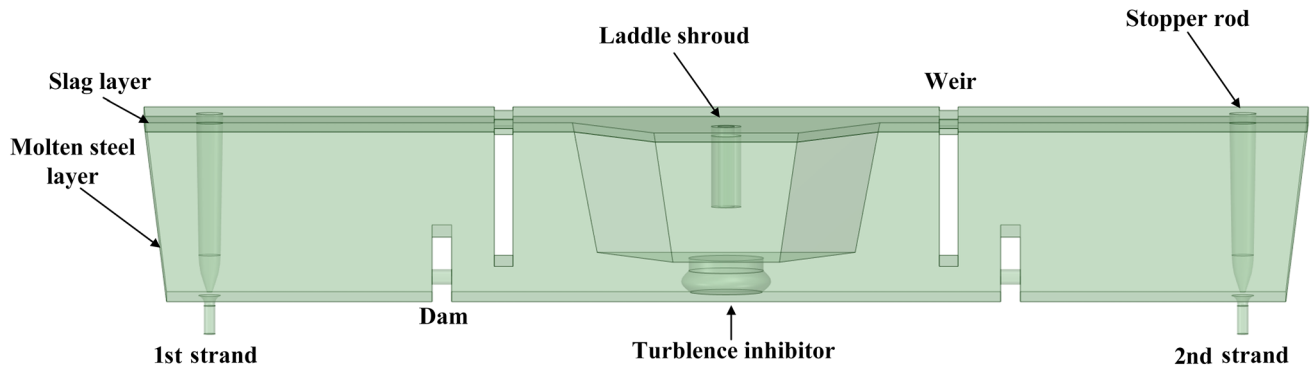
Fig. 1 Schematic diagram of two-strand tundish model

Table 1 Operating parameter of tundish

Casting condition	Value
Slab cross section/(mm×mm)	1020×200
Casting speed/(m min^{-1})	2.2
Height of steel at steady-state/mm	922
Thickness of slag layer/mm	70
Distance of stopper-rod to bottom of tundish/mm	20
Submergence depth of LS/mm	360
Inner diameter of LS/mm	90
Inner diameter of SEN/mm	60

at the end of sequence are obtained by the flow field in the same tundish under the steady-state casting. The velocities of molten steel during steady-state casting at the outlets and inlet are calculated according to the casting speed and slab section:

$$V_{\text{inlet}} = \frac{S \times v_{\text{cast}} \times N}{S_{\text{LS}}} \tag{11}$$

$$V_{\text{outlet}} = \frac{S \times v_{\text{cast}}}{S_{\text{SEN}}} \tag{12}$$

where V_{inlet} and V_{outlet} are the velocity at computational inlet and outlets, respectively, m s^{-1}; S is the cross-sectional area of the slab, m^2; v_{cast} is the casting speed, m s^{-1}; S_{LS} and S_{SEN} are the inner cross-sectional area of the LS
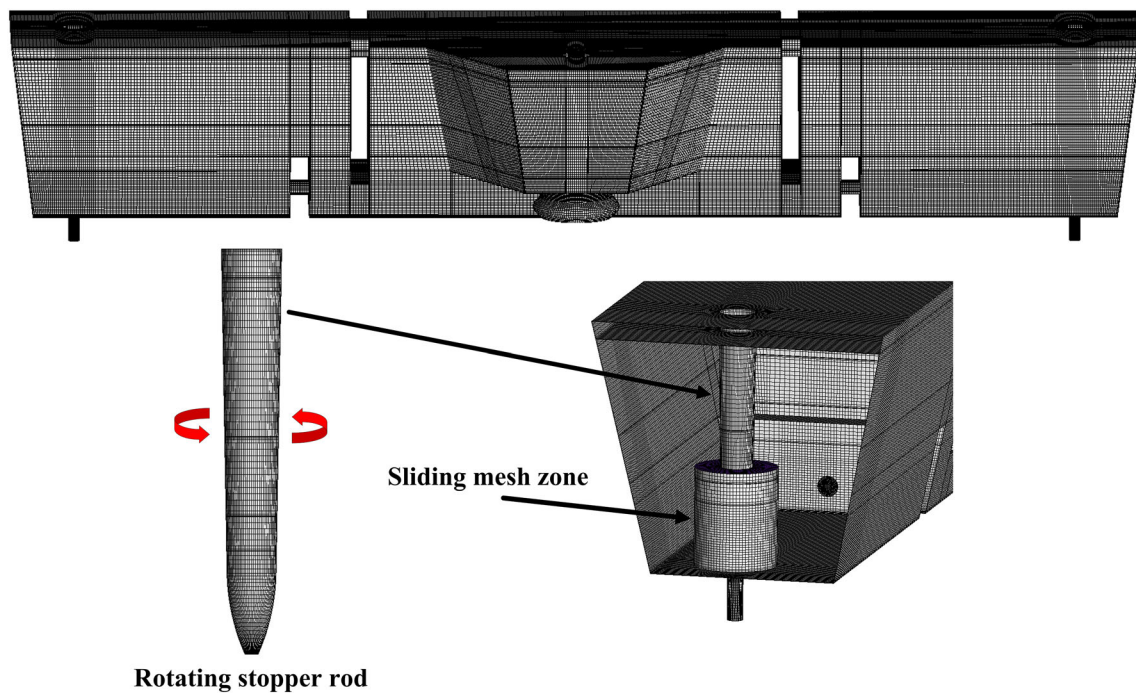

Fig. 2 Computational mesh of whole tundish

and SEN, respectively, m^2; and N is the number of strands, $N = 2$.

If both steady-state casting and transient casting use the LES for calculation, it will consume too much computing resources. The research on the RANS model in the steady flow field of the tundish is very mature, and many scholars have also verified it by conducting water model experiments. Therefore, in this study, the standard k–ε model was used to calculate the flow field of the steady state, and then switched the turbulent model to the LES model and patched on the slag phase and the molten steel phase in the calculation of multiphase behaviors during the draining process at the end of tundish casting sequence.

The shared topology is used for the mesh of upper and lower computational domains. The boundary conditions of the simulation are set as follows:

(1) During steady-state computation, the interface between the upper and lower computation domains is set as wall. The inlet is set as velocity inlet and velocity distribution of inlet is regarded as uniform. The value of inlet velocity can be calculated by Eq. (11).

(2) During the draining process at the end of sequence, the interface between the upper and lower computational domains is set as interior, so that the slag and air can flow downward. The boundary conditions for the computational inlet and the free-surface are set to be pressure inlet.

(3) The velocity outlet boundary condition is applied for the computational outlet during both steady-state casting and the end of the tundish casting sequence.

(4) The sliding mesh technique is used in the calculations when the stopper-rods rotate. The contact surface between the rotating and non-rotating domains in the vicinity of the stopper-rod is set as interface.

(5) The rest of the walls in the tundish are non-slip walls.

2.4 Numerical solution procedure

The calculations were solved by commercial software Ansys Fluent 2020. For transient multiphase flow at the end of casting sequence, it is more suitable to use the PISO algorithm to couple the pressure term and the velocity term. It can also reduce the number of iterations of the momentum equation and increase the computational efficiency. Since there will be a free-surface vortex at the end of the tundish casting sequence, and there are strong bending areas near the nozzle, it is more suitable to use PRESTO! for pressure interpolation. The bounded central differencing scheme was applied to the functions of

momentum. Compressive was used for volume fraction interpolation. The time step is 0.005 s. The convergence residual criterion is less than 10^{-5}. The calculated physical parameters of the materials used are shown in Table 2. The simulations were run on a server host (Intel Xeon(R) platinum 8375C@2.90 GHz*2) with 256G running memory. The whole work of calculating the draining process in the tundish from steady-state level to free-surface vortex formation by the LES–VOF coupled model takes about 40 days to complete.

3 Model validation

A simple model similar to a single-strand tundish was used to validate the LES–VOF coupled model for the three-phase flow of steel–slag–air at the end of tundish casting sequence. The ratio of the numerical simulation model to the simple model is 1:1, and all the casting conditions are kept the same. The schematic diagram of the water model experimental platform and the initial experimental conditions are shown in Fig. 3.

In the water model experiment and numerical simulation, the experimental materials used are vacuum pump oil, water and air. The physical parameters of the experimental materials are shown in Table 3. The initial conditions of the water model experiments and numerical simulations were the same. Both the water in the model was first allowed to reach a steady-state flow at an outlet and inlet flow rate of 14.6 L min^{-1}. After that, the vacuum pump oil with the thickness of 2 cm was added into the tundish. When the flow of water and oil reaches steady-state, the water was allowed to flow out at a constant flow rate of 14.6 L min^{-1}.

Figure 4 shows the comparative validation of the penetration height of free-surface vortex measured by water model experiment and calculated by numerical simulation. The penetration height of free-surface vortex means the height of water when free-surface vortex penetrates

Table 2 Physical parameters of molten steel, slag and air

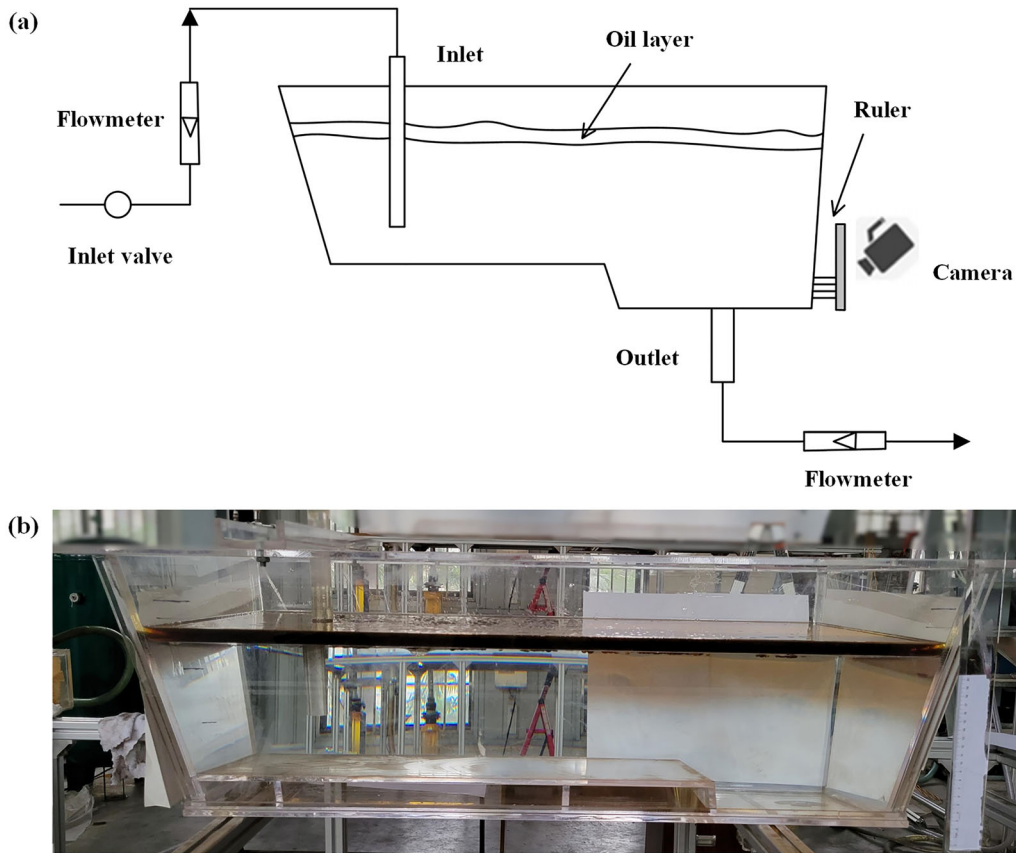| Parameter	Value
Molten steel density/(kg m^{-3})	7000
Molten steel viscosity/(kg m^{-1} s^{-1})	0.0062
Slag density/(kg m^{-3})	2800
Slag viscosity/(kg m^{-1} s^{-1})	0.2
Air density/(kg m^{-3})	1.225
Air viscosity/(kg m^{-1} s^{-1})	1.7894×10^{-5}
Surface tension coefficient of air–steel/(N m^{-1})	1.6
Surface tension coefficient of air–slag/(N m^{-1})	0.38
Surface tension coefficient of steel–slag/(N m^{-1})	1.4

Fig. 3 Schematic diagram of water model experiment (**a**) and initial condition (**b**)

Table 3 Physical parameters of experimental materials

Material	Color	Density/(kg m^{-3})
Water	Colorless and clear	998
Vacuum pump oil	Yellow and clear	890
Air	Colorless and clear	1.225

through the outlet. It can be seen that the penetration height of the free-surface vortex calculated by LES–VOF coupled model and water experiment are 22.0 and 22.5 mm, respectively. The error between simulation and experiment is only about 2.22%. The current numerical can accurately simulate the formation and suppression process of vortex at the end of tundish casting sequence.
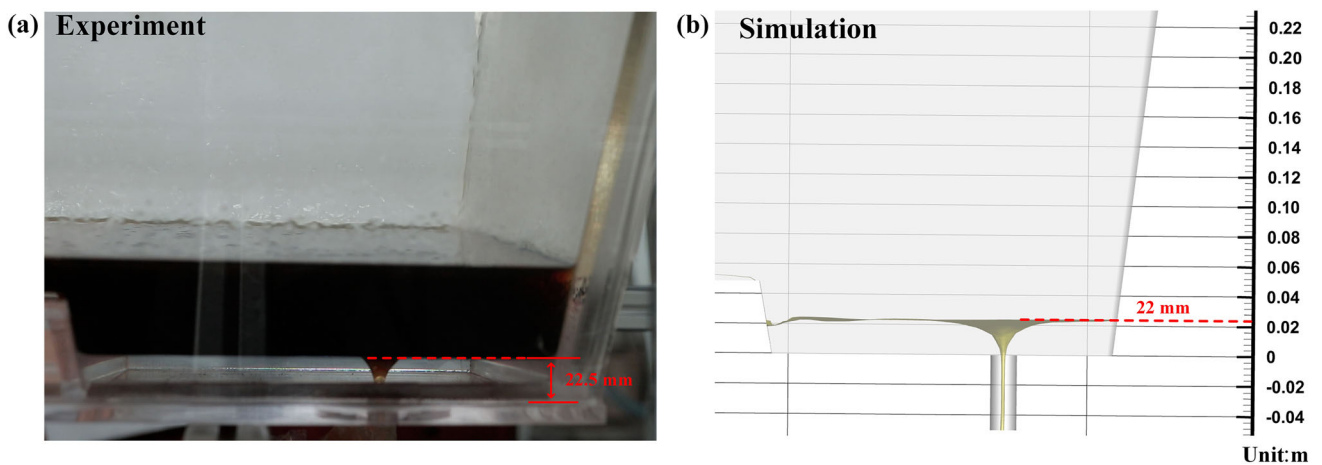
Fig. 4 Penetration height measured by water model experiment and calculated by LES–VOF coupled model. **a** Water model experiment; **b** simulation result
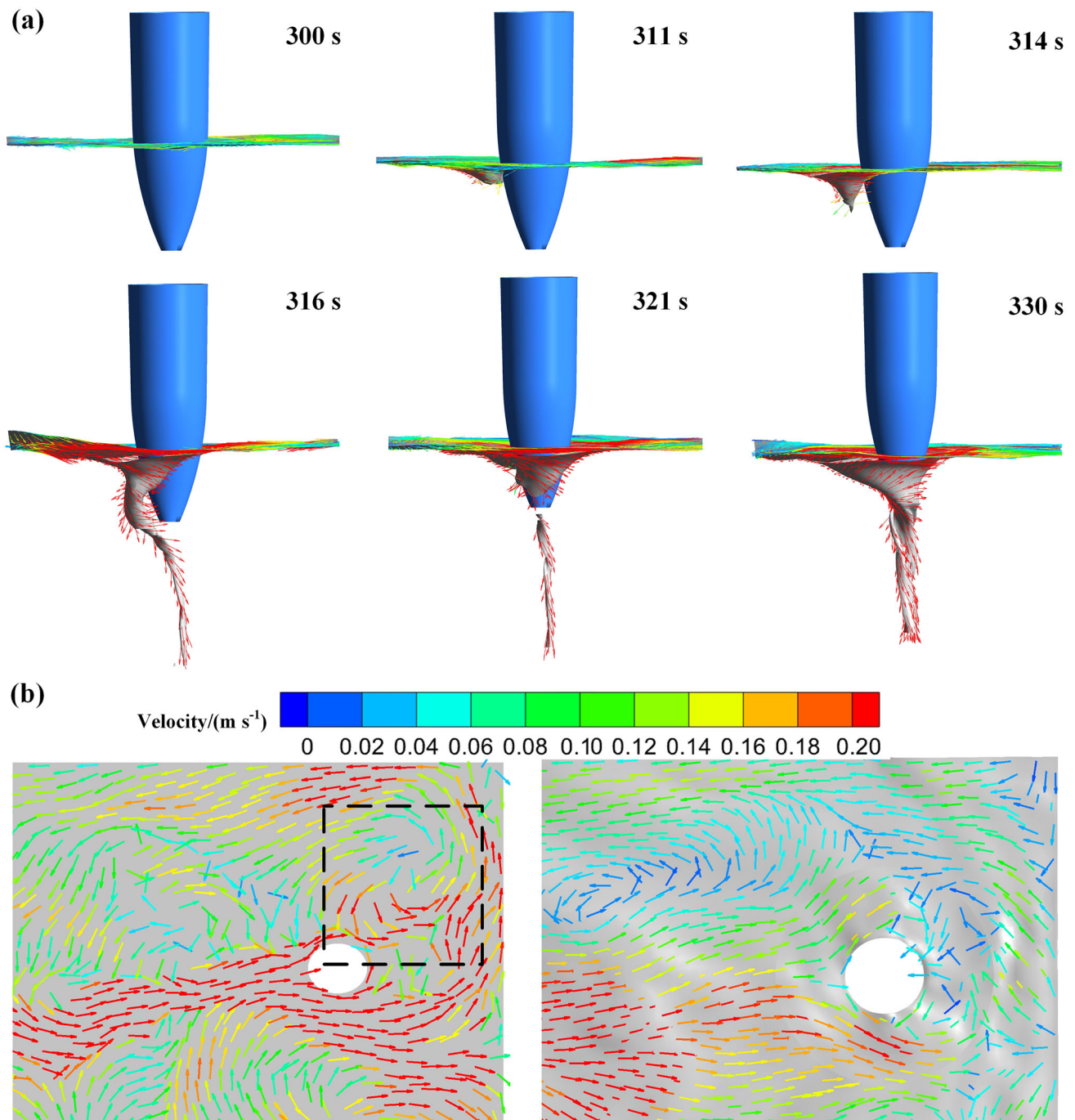
Fig. 5 Evolution of free-surface vortex. **a** Shape of free-surface vortex at different draining time; **b** velocity vector of molten steel at $z = 0.1$ m and slag–steel interface at 300 s

4 Results and discussion

4.1 Formation mechanism of free-surface vortex

After calculating the steady-state flow field by using the standard k–ε model, the LES model is switched to calculate the process at the end of casting sequence without rotation of the stopper-rod, to obtain the direction of rotation of the

free-surface vortex above each SEN and the start time of the vortex formation. Then, the stopper-rod is rotated to disturb the flow of the molten steel above the SEN when the vortex is about to be formed. The suppression effect of different rotating speeds was evaluated and compared by the calculation of the LES–VOF coupled model.

The start time ($t = 0$ s) in the transient calculation shows that the time of LS being closed and at the beginning of
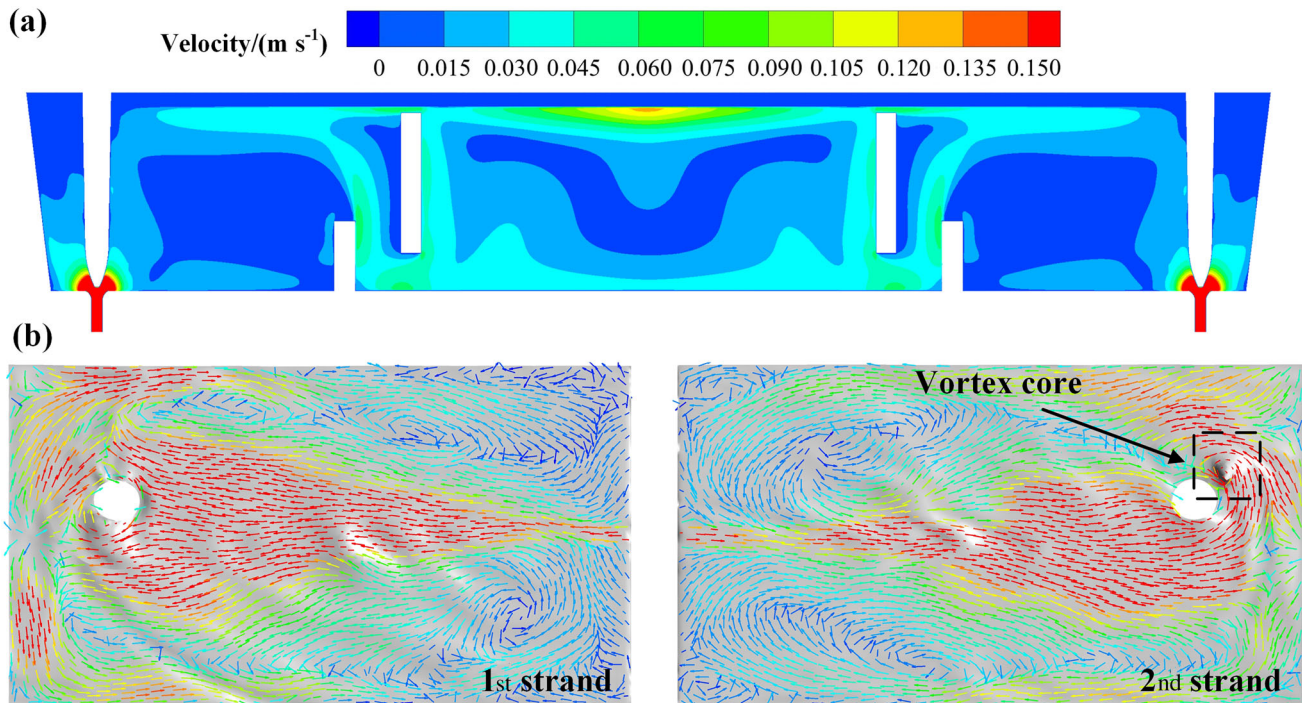
Fig. 6 Asymmetric flow field of two-strand tundish. **a** Velocity contour in vertical section; **b** velocity vector of slag–steel interface above 1st strand and 2nd strand at 314 s

draining process at the end of sequence. Figure 5 presents the three-dimensional evolution of topography of free-surface vortex above the 2nd strand with draining time at the end of sequence when the stopper-rod is not rotated, and the velocity vector of molten steel at $z = 0.1$ m (z represents the vertical direction extending perpendicularly from the bottom of the tundish) and slag–steel interface at 300 s. The bottom of tundish is $z = 0$ m. It can be seen that the energy for the formation and development of the free-surface vortex comes from the gravity of the molten steel itself. The area near the bottom of the SEN is the source of power for the development of the free-surface vortex. Due to the inner structure of the tundish, the diversion hole on the dam and the SEN are not in the horizontal line. The molten steel flowing out from the diversion hole on the dam to the outlet with a certain tangential velocity is relative to the center of the SEN. The process of vortex formation follows the conservation of angular momentum, which makes the rotating speed faster and faster. Due to the continuity of the molten steel flow, the rotation of the molten steel near the SEN will drive the rotation of the molten steel above, and the vortex core starts to form on the slag–steel interface. At the presence of the stopper-rod, the vortex core was not formed at first directly above the SEN, but near the stopper-rod. As the vortex develops, the flow rate at the center of the vortex increases. According to Bernoulli's theorem, the center of the liquid surface will gradually depress and pass through

the SEN. As the liquid level continued to decrease, the vortex continued to develop, and finally the core of the vortex directly moved to the SEN.

4.2 Suppression of vortex by rotating stopper-rod

Figure 6 shows the asymmetric flow field in the two-strand tundish. It can be seen from Fig. 6a that the left and right parts of the flow field are basically symmetrical when calculating the steady-state casting process in the tundish by the standard k–ε model. However, as shown in Fig. 6b, the asymmetric flow field in the tundish is gradually serious with the steel continuously draining out through. At 314 s, there is already a vortex core formed above the 2nd strand, while there is no vortex core formed above the 1st strand. The formation time of free-surface vortex above the 2nd strand is earlier than that above the 1st strand. Eventually, the direction of free-surface vortex formed above the two strands is opposite. The direction of the vortex formed above the 1st strand is clockwise, and the direction of the vortex formed above 2nd strand is counterclockwise.

It can be seen from Fig. 5a that the free-surface vortex did not form at 300 s. In order to disturb the formation of vortex above the SEN, rotating stopper-rods with reverse rotation before the free-surface vortex formed. Reverse rotation of the two stopper-rods is performed at 290 s, with counterclockwise rotation of stopper-rod above the 1st

strand and clockwise rotation of stopper-rod above the 2nd strand. The stopper-rod with rotating speeds of 30, 60, 90, and 120 r/min are considered and compared for suppressing the free-surface vortex in the tundish at the end of casting sequence.

Figure 7 shows the velocity vectors at slag–steel interface above the 1st and 2nd strand at 300 s with different rotating speeds of stopper-rod. It can be seen from Fig. 7 that when the stopper-rod is not rotating, the molten steel flows through the stopper-rod and splits into two streams due to the obstruction of the stopper-rod. The upper flow stream collides with the steel bouncing back from the wall of tundish, which causes a small closed-loop vortex formed in the upper right corner of the stopper-rod, which is the source of the vortex core formation. When the stopper-rod rotates, it leads to a rotating flow of steel above the SEN. The flow which is originally able to flow from below the stopper is obstructed by the rotating flow, and a large vortex formed in the lower left corner of the stopper. As the rotating speed increases, the velocity of rotating flow exceeds 0.15 m s^{-1}, and the lower stream is more difficult to flow forward. Without the lower stream flowing through the stopper-rod, the upper right corner of the stopper-rod did not form a small closed-loop vortex, which disturbed the formation of the vortex core and delayed the formation of the vortex.

Figure 8 shows the velocity vector at the iso-surface ($\alpha_{slag} = \alpha_{molten\ steel} = 0.5$, α_{slag} and $\alpha_{molten\ steel}$ represent the volume fractions of slag and molten steel, respectively) at 340 s with different rotating speeds of stopper-rods. It can be seen in Fig. 8, the direction of the free-surface vortex at 0 and 30 r/min is basically the same. When the rotating speed of stopper-rod increases to 60 r/min, the direction of vortex rotation above the 1st strand is gradually changing from clockwise to counterclockwise due to the late formation of vortex core and the suppressing influence of rotating stopper-rod. Since the vortex core above the 2nd strand formed earlier than the 1st strand, the vortex above the 2nd strand is not so much affected by the rotating stopper-rod, and the rotating direction is changing. When the rotating speed increases to 90 and 120 r/min, due to the high rotating speed of the stopper-rod, the molten steel around the stopper-rod has formed a small rotating flow field, and the rotating direction is the same as the rotating direction of the stopper-rod. With the liquid level dropping, the molten steel flowing from the diversion hole on the dam meets the rotating flow field around the stopper-rod and then moves together with the rotating flow field around the stopper-rod. It is beneficial to the formation of free-surface vortex, and the suppression effect of rotating stopper-rods is obviously inhibited. Finally, the rotating direction of vortex at 90 and 120 r/min is the same as the rotating direction of the stopper-rod.

By monitoring the mass flow rate of slag over time at the outlet of each strand, the start time of slag entrainment and the time of fast slag entrainment can be obtained. The time of fast slag entrainment is the time when the mass flow rate of the slag monitored at the SEN increases rapidly, which is almost the time when the free-surface vortex penetrates the SEN. Figure 9 presents the mass flow rate of slag phase at the 1st strand and the 2nd strand with draining time sunder different rotating speeds of stopper-rod. As shown in Fig. 9, when the stopper-rod did not rotate, the start time of the slag entrainment at the 2nd strand is 8 s earlier than that at the 1st strand. The time of fast slag entrainment at the 2nd strand is 12 s earlier than that at the 1st strand. After the stopper-rod rotating, the start time of slag entrainment and the time of fast slag entrainment of each rotating speed were all later than the no-rotation case. Especially for the 2nd strand whose vortex formation is earlier, the time of fast slag entrainment is almost 20 s later. It can also be seen from Fig. 9 that the rotation of the stopper rod can effectively delay the time of fast slag entrainment and reduce the slag entrainment. Compared to other cases, the reduced mass of slag entrainment is the most when the rotating speed is 60 r/min.

Figure 10 shows the height of molten steel level and mass of residual steel in the tundish when the free-surface vortex penetrates under different rotating speeds of stopper-rod. For the 2nd strand where the free-surface vortex is formed earlier, as long as the rotation of the stopper-rod disturbs the formation of the vortex above the SEN, the critical height of the vortex formation will decrease. When the stopper-rod did not rotate, the critical height of the free-surface vortex above the 1st strand and the 2nd strand is 9.7 and 13.8 cm, respectively. The mass of residual steel in the tundish is 5.3 t. When the rotating speeds are 30, 60, 90 and 120 r/min, the critical height of the free-surface vortex above the 1st strand is decreased to 6.1, 5.3, 7.8 and 7.3 cm, respectively. The drop of the critical height of the free-surface vortex above the 2nd strand is significant. When the rotating speeds are 30, 60, 90 and 120 r/min, the critical height of the free-surface vortex above the 2nd strand are 7.3, 4.7, 6.3 and 7.4 cm, respectively. Taking the earliest penetration time of the two strands as the boundary, by monitoring the flow rate of molten steel flowing out of each strand before the boundary, the total mass of molten steel flowing out of each strand is counted, and the mass of residual steel in the tundish is calculated. It is obvious that rotating the stopper-rod can significantly reduce the mass of residual steel in the tundish at the end of the sequence, about 1.6 t when the rotating speed is 30, 90, and 120 r/min. When the rotating speed of stopper-rod is 60 r/min, it can reduce the mass of residual steel of about 2 t.
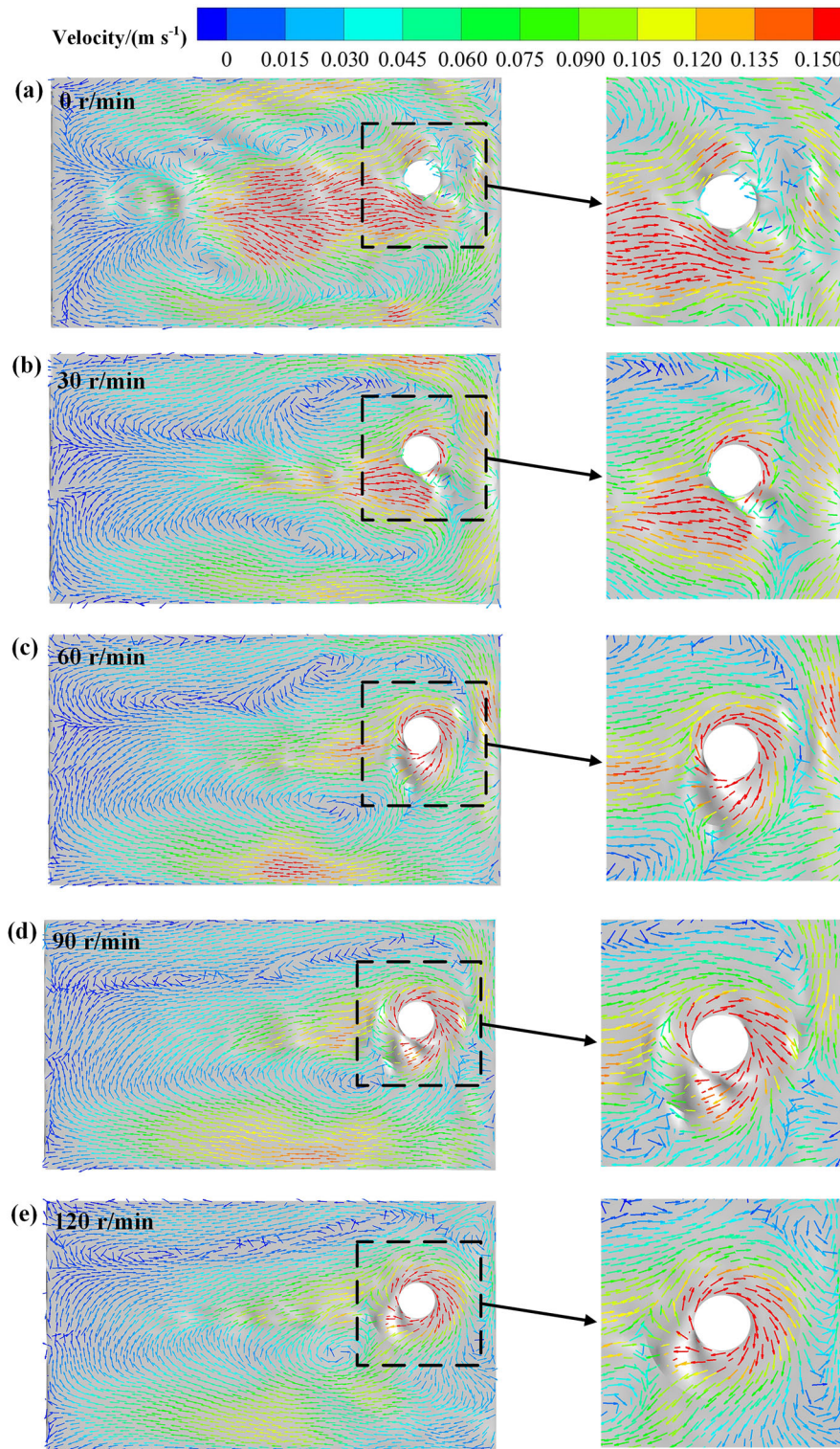
Fig. 7 Velocity vector of slag–steel interface above 2nd strand at 300 s with different rotating speeds. **a** 0 r/min; **b** 30 r/min; **c** 60 r/min; **d** 90 r/min; **e** 120 r/min
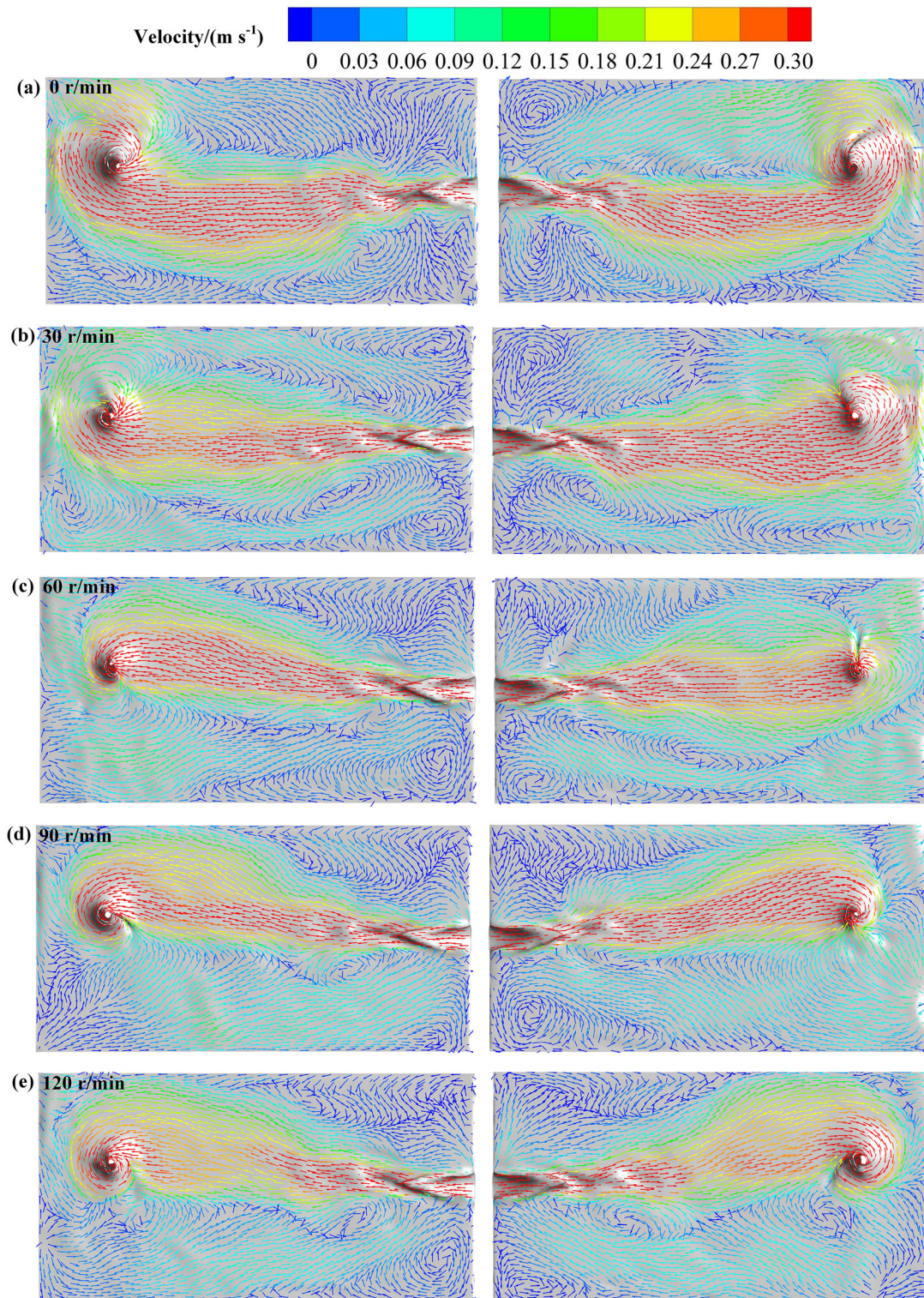
Fig. 8 Velocity vector of iso-surface ($\alpha_{slag} = \alpha_{molten\ steel} = 0.5$) above 1st strand (left) and 2nd strand (right) at 340 s with different rotating speeds. **a** 0 r/min; **b** 30 r/min; **c** 60 r/min; **d** 90 r/min; **e** 120 r/min
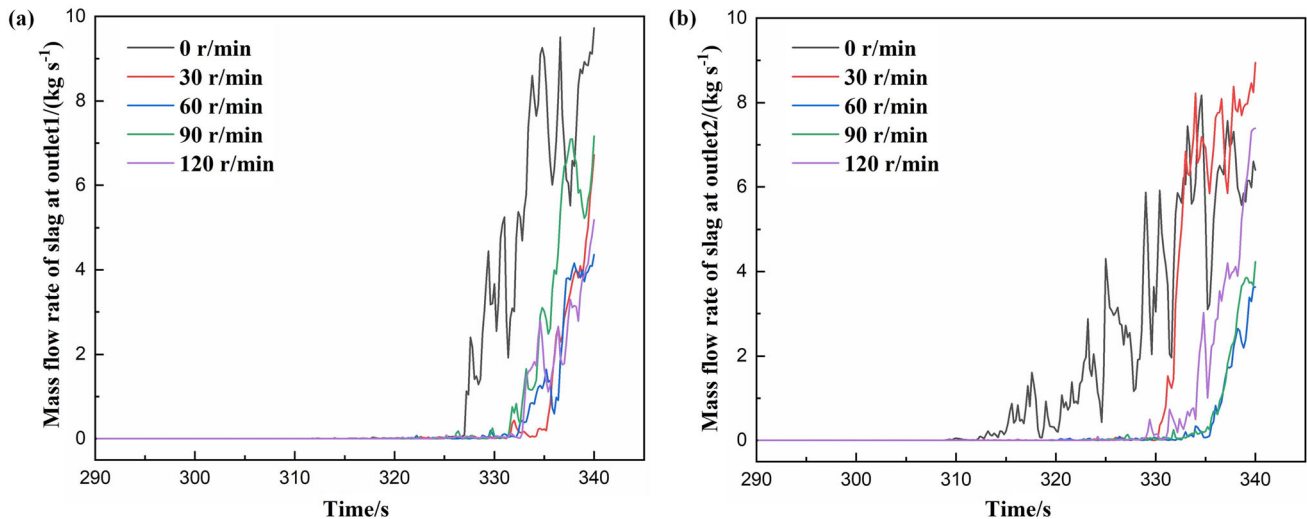
Fig. 9 Variations of mass flow rate of slag phase with draining time under different rotating speeds of stopper-rod. **a** 1st strand; **b** 2nd strand
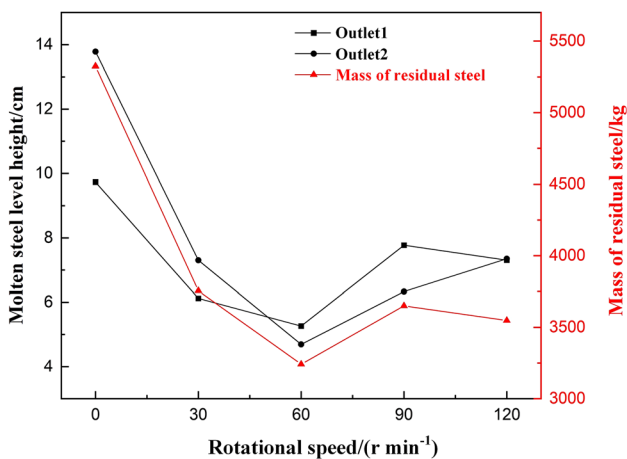
Fig. 10 Height of molten steel level and mass of residual steel at different rotating speeds

5 Conclusions

1. The numerical results of critical height of free-surface vortex are consistent with experimental results. The current LES–VOF coupled model is suitable for simulating the formation and suppression of free-surface vortex in the tundish at the end of casting sequence.

2. When the molten steel flowing toward the SEN, it has a certain tangential velocity after passing through the diversion hole of dam. It will prompt the formation of vortex core. Due to conservation of angular momentum, the velocity of vortex center will be faster and faster. Finally, the center liquid surface will gradually concave and penetrate into the SEN eventually.

3. When the stopper-rod did not rotate, the mass of residual steel is 5.3 t and the critical height of free-surface vortex of the 1st strand and the 2nd strand is 9.7 and 13.8 cm, respectively. This is attributed to the uncertainty of turbulence, and the flow field of the two-strand tundish appears asymmetric at the end of the sequence.

4. The rotating stopper-rod can effectively disturb the formation of vortex and reduce the critical height of the free-surface vortex formation, especially for the 2nd strand. When the rotating speeds are 30, 60, 90 and 120 r/min, the critical height of the free-surface vortex above the 2nd strand is 7.3, 4.7, 6.3 and 7.4 cm, respectively. When the rotating speed of stopper-rod is 60 r/min, compared with no-rotation case, the mass reduction of residual steel in the tundish reaches 2.0 t.

5. It is worth to further investigate the optimum process conditions for the rotating stopper-rod. It is planned to study the effect of different shapes of stopper-rod, different start time of rotation, different rotation time and other factors on the suppression of the free-surface vortex in the next step.

Declarations

Conflict of interest On behalf of all authors, the corresponding author states that there is no conflict of interest.

References

[1] Y. Yin, J. Yang, J. Zhang, L. Tang, J. Mater. Res. Technol. 23 (2023) 1781–1791.

[2] C. Huang, Y. Sun, W. Liu, J. Li, S. Yang, J. Dong, Materials 16 (2023) 3209.

[3] A. Gupta, R. Kumar, R.K. Singh, Met. Mater. Int. 28 (2022) 1246–1256.

[4] G. Solorio-Diaz, A. Ramos-Banderas, J. de J. Barreto, R.D. Morales, Steel Res. Int. 78 (2007) 248–253.

[5] Z. Li, M. Zhang, F. Zhou, Y. Lu, X. Zhang, H. Gu, Ironmak. Steelmak. 49 (2022) 1039–1047.

[6] H.X. Li, Q. Wang, H. Lei, J.W. Jiang, Z.C. Guo, J.C. He, ISIJ Int. 54 (2014) 1592–1600.

[7] H. Tang, Y. Liang, Acta Metall. Sin. 52 (2016) 519–528.

[8] Y. Ruan, Y. Yao, S. Shen, B. Wang, J. Zhang, J. Huang, Steel Res. Int. 91 (2020) 1900616.

[9] M. Xuan, M. Chen, K. Zhang, X. Hua, The Minerals, Met. Mater. Ser. Springer, Cham, Germany, 2021.

[10] Q. Wang, L. Wang, H. Li, J. Jiang, X. Zhu, Z. Guo, J. He, Acta Metall. Sin. 54 (2017) 959–968.

[11] B. Khadem Rabe, S.H. Ghoreishi Najafabadi, H. Sarkardeh, Proc. Inst. Civ. Eng. Water Manag. 171 (2018) 18–29.

[12] X. Gao, H. Zhang, J. Liu, B. Sun, Y. Tian, Eng. Appl. Comput. Fluid Mech. 12 (2018) 182–194.

[13] D.Y. Sheng, Z. Zou, Metals 11 (2021) 208.

[14] K. Takahashi, M. Ando, T. Ishii, ISIJ Int. 54 (2014) 304–310.

[15] X. Li, B. Li, Z. Liu, D. Wang, T. Qu, S. Hu, C. Wang, R. Gao, Metall. Mater. Trans. B 52 (2021) 3246–3264.

[16] X. Li, B. Li, Z. Liu, R. Niu, Y. Liu, C. Zhao, C. Huang, H. Qiao, T. Yuan, Metals 9 (2018) 7.

[17] X. Zhao, X. Li, J. Zhang, Metals 11 (2021) 374.

[18] Q. Zhou, T. Zhu, L. Zhang, W. Chen, T. Yuan, Z. Liu, Iron and Steel 57 (2022) No. 7, 68–78.

[19] W. Chen, L. Zhang, Metall. Mater. Trans. B 52 (2021) 528–547.

[20] Q. Li, L. Zhang, W. Chen, Y. Wang, Z. Zhao, J. Zhang, Chinese Journal of Engineering 44 (2022) 690–702.

[21] W. Chen, L. Zhang, Q. Ren, Y. Ren, W. Yang, Metall. Mater. Trans. B 53 (2022) 1446–1461.

[22] J. Zhang, S. Yang, J. Li, W. Yang, Y. Wang, X. Guo, ISIJ Int. 55 (2015) 1684–1692.

[23] N. Alkishriwi, M. Meinke, W. Schröder, A. Braun, H. Pfeifer, Steel Res. Int. 77 (2006) 565–575.

[24] A. Leonard, Advances in Geophysics 18 (1975) 237–248.

[25] Ansys Inc. Fluent, Ansys. 19.0 User's Guide, 2019.

[26] J. Zhang, Q. Liu, Z. Xin, B. Lu, J. Zhang, J. Li, IOP Conf. Ser.: Mater. Sci. Eng. 668 (2019) 012007.

[27] F. Nicoud, F. Ducros, Flow Turbul. Combust. 62 (1999) 183–200.

[28] H. Zhang, J. Wang, Q. Fang, G. Wu, P. Zhao, H. Ni, Steel Res. Int. 93 (2022) 2100536.